

**Wavelet Space-Scale-Decomposition Analysis of QSO's Ly α
Absorption Lines: Spectrum of non-Gaussianity**

Jesus Pando and Li-Zhi Fang

Department of Physics, University of Arizona, Tucson, AZ 85721

arXiv:astro-ph/9606005v1 3 Jun 1996

Abstract

Using a discrete wavelet based space-scale decomposition (SSD), the spectrum of the skewness and kurtosis is developed to describe the non-Gaussian signatures in cosmologically interesting samples. Because the basis of the discrete wavelet is compactly supported, the one-point distribution of the father function coefficients (FFCs) taken from one realization is a good estimate of the probability distribution function (PDF) of density fields if the “fair sample hypothesis” holds. These FFC one-point distributions can also avoid the constraints of the central limit theorem on the detection of non-Gaussianity. Thus, the FFC one-point distributions are effective in detecting non-Gaussian behavior in samples such as non-Gaussian clumps embedded in a Gaussian background, regardless of the number or number density of the clumps. We demonstrate that the non-Gaussianity spectrum can reveal not only the magnitudes, but also the scales of the non-Gaussianity.

Also calculated are the FFC one-point distributions, skewness and kurtosis spectra for real data and linearly simulated samples of QSO Ly α forests. When considering only second and lower order of statistics, such as the number density and two-point correlation functions, the simulated data show the same features as the real data. However, the kurtosis spectra of samples given by different models are found to be different. On the other hand, the spectra of skewness and kurtosis for independent observational data sets are found to be the same. Moreover, the real data are significantly different from the non-Gaussianity spectrum of various possible random samples. Therefore, the non-Gaussian spectrum is necessary and valuable for model discrimination.

Subject headings: cosmology: large-scale structure of Universe – quasars: absorption lines

1. Introduction

This is our third paper on developing the discrete wavelet transform (DWT) into a powerful space-scale decomposition (SSD) method for the analysis of the large scale structures. The first two papers studied 1) identification of clusters (Pando & Fang 1996, hereafter PF1); 2) determination of power spectrum of density perturbations (Pando & Fang 1995, hereafter PF2). In this paper, a method of detecting non-Gaussian behavior via the DWT, and its application to both simulated and observational data of QSO's Ly α absorption lines is presented.

There are important motivations for studying the non-Gaussianity of cosmic distributions. In standard inflation/dark matter cosmology, primordial perturbations generated in the inflationary era are scale-free and Gaussian. The subsequent evolution of the density perturbations in the linear regime destroys the scaling of the spectrum, but the density field remains Gaussian. Deviations from the Gaussian state in the cosmic density distribution occur first because of the non-linear evolution caused by the gravitational instability of baryonic and dark matter. In this highly non-linear evolutionary stage the density field should be very non-Gaussian. Additionally, even when the background density distribution is Gaussian, the distribution of visible objects may be non-Gaussian if their distribution is biased with respect to the background distribution. However, detection of non-Gaussian behavior has, in many respects, been inconclusive. For instance, no deviations from Gaussian behavior were found in the QDOT-IRAS redshift survey (Feldman, Kaiser & Peacock 1994), and even for simulation samples in which a strong non-linear evolution is part of the model, the one point distribution function was found to be consistent with a Gaussian distribution (Suginohara & Suto 1991).

It is generally believed that the failure in detecting non-Gaussian behavior is due partially to the constraint imposed on Fourier techniques by the central limit

theorem when applied to the one point distribution function. It is well known from the central limit theorem of random fields (Adler 1981; Ivanonv & Leonenko 1989) that if the universe consists of a large number of dense clumps, and those clumps are independent, the real and imaginary components of each individual Fourier mode are Gaussian distributed although the probability distribution functions (PDF) of the field itself are highly non-Gaussian. If the clumps are not distributed independently, but are correlated, the central limit theorem still holds if the two-point correlation function of the clumps approaches zero sufficiently fast (Fan & Bardeen 1995). The central limit theorem holds even for processes that are a time (or space) average of a non-Gaussian distribution as long as the ratio of the sampling time to the scale of the fluctuation increases (Adler 1981). For these reasons, the one-point distribution function of Fourier modes is not a sensitive enough measure to detect deviations from Gaussian behavior.

This difficulty can be overcome by using the count in cell (CIC) method because the CIC is based on localized window functions, which in essence, keep the sampling time to scale of fluctuation ratio mentioned above from increasing. Thus, the CIC statistic is not restricted by the central limit theorem. CIC has succeeded in detecting non-Gaussian signatures (Hamilton 1985; Alimi, Blanchard & Schaeffer 1990; Gaztañaga & Yokoyama 1993; Bouchet et al. 1993; Kofman et al. 1994; Gaztañaga & Frieman 1994). However, it has been found that the CIC results are dependent on the parameters of the window function (Juszkiewicz et al. 1993). This is because non-Gaussian distributions are generally scale-dependent, and therefore, a window function with a different scale will obtain different degrees of non-Gaussian behavior (Yamada & Ohkitani 1991). The results obtained via a CIC analysis will be a superposition of information on scales larger than the size of the window. Therefore, in order to completely describe the non-Gaussianity of density fields and object distributions, it is very necessary to have an effective and uniform measure of the scale-dependence

or *spectrum* of non-Gaussianity.

In the first part of this paper, we will study a method of detecting the non-Gaussian spectrum by the discrete wavelet SSD. As with the CIC, the bases of discrete wavelet SSD are localized, and therefore, avoid the restrictions of central limit theorem. On the other hand, the SSD modes are orthogonal and complete and no scale mixing occurs. It is easy to decompose the contribution of structures on various scales to the non-Gaussianity. Hence, one can expect that a discrete wavelet SSD will be effective in detecting the non-Gaussianity spectrum of large scale structures.

In the second part of the paper, we calculate the non-Gaussianity of real and simulated samples of QSO Ly α forests. Most 2nd order statistical studies, such as the two-point correlation function or power spectrum, have failed to detect structure in the distributions of QSO Ly α forests. On the other hand, statistics not based on the power spectrum or 2 point correlation function have indicated that these distributions should have structure (see, for example, Duncan, Ostriker, & Bajtlik 1989; Liu and Jones 1990; Fang 1991). These examples illustrate that it is necessary to go beyond the 2nd order statistics, that is, to look at non-Gaussian behavior.

2. Method

2.1 Wavelet expansion

We use the notation introduced in PF1 and PF2. Consider a one-dimensional density field $\rho(x)$ over a range $0 \leq x \leq L$. It is convenient to use the density contrast defined by

$$\delta(x) = \frac{\rho(x) - \bar{\rho}}{\bar{\rho}} \quad (1)$$

where $\bar{\rho}$ is the mean density in this field. To express $\delta(x)$ in a Fourier expansion, we take the convention

$$\delta(x) = \sum_{n=-\infty}^{\infty} \delta_n e^{i2\pi nx/L} \quad (2)$$

with the coefficients computed by

$$\delta_n = \frac{1}{L} \int_0^L \delta(x) e^{-i2\pi nx/L} dx. \quad (3)$$

Now contrast this with the wavelet expansion of the density $\rho(x)$ (Meyer 1993). We first assume that $\rho(x)$ is an L periodic function defined on space $-\infty < x < \infty$ (this condition may actually be relaxed.). The wavelet expansion is then given by (Daubechies 1992, PF2)

$$\rho(x) = \sum_{m=-\infty}^{\infty} c_{0,m} \phi_{0,m}(x) + \bar{\rho} \sum_{j=0}^{\infty} \sum_{l=-\infty}^{\infty} \tilde{\delta}_{j,l} \psi_{j,l}(x) \quad (4)$$

where $\bar{\rho}$ is the mean density. $c_{0,m}$ is the mother function coefficient (MFC) on scale $j = 0$ and position l , while $\tilde{\delta}_{j,l}$ is the father function coefficient (FFC) on scale j and position l . The MFC and FFC are calculated by the inner products as

$$c_{j,m} = \int_{-\infty}^{\infty} \rho(x) \phi_{j,m}(x) dx \quad (5)$$

$$\tilde{\delta}_{j,l} = \int_{-\infty}^{\infty} \delta(x) \psi_{j,l}(x) dx \quad (6)$$

where $\delta(x)$ is the density contrast given by eq.(1). The mother function $\phi_{j,m}(x)$ and father function $\psi_{j,l}$ are given, respectively, by $\phi_{j,m}(x) = (2/L)^{1/2} \phi(2^j x/L - m)$ and $\psi_{j,l}(x) = (2^j/L)^{1/2} \psi(2^j x/L - l)$, where $\phi(x)$ is the scaling function, and $\psi(x)$ the basic wavelet. The $\phi(x)$ and $\psi(x)$ must meet certain admissibility conditions (Farge 1992). The Daubechies 4 wavelets meet all these conditions and are the discrete wavelet bases used in this paper.

2.2 Restriction of central limit theorem

Among the various methods of detecting Gaussian deviations, the one-point distribution of the density field is especially important because the probability distribution functions (PDF) of density fields can be directly determined by the one-point

distribution. That is, the one-point distribution can detect not only the deviation from a Gaussian distribution, but can also detect the non-Gaussian PDF itself.

Let us consider the non-Gaussianity of density fields $\delta(x)$ consisting of randomly distributed non-Gaussian clumps. In this case, eq.(3) shows that for large L the Fourier amplitudes, δ_n , are given by a superposition of a large number of non-Gaussian distributions. According to the central limit theorem, the distribution of δ_n will be Gaussian when the total number of clumps is large. Thus, in general, the non-Gaussianity of distributions of randomly distributed clumps can not be seen from the one-point distribution of the Fourier modes, δ_n , even if the PDF function of clumps is highly non-Gaussian.

On the other hand, the father functions, $\psi_{j,l}(x)$, are localized. If the scale of the clump is d , eq.(6) shows that the FFC, $\tilde{\delta}_{j,l}$, with $j = \log_2(L/d)$, is determined only by the density field in a range containing no more than one clump. That is, FFCs are not given by a superposition of a large number of non-Gaussian variables, but determined by one, or at most, a few non-Gaussian processes. The one point distribution of the FFC, $\tilde{\delta}_{j,l}$, avoids the restriction of the central limit theorem, and is able to detect non-Gaussianity, regardless the total number of the clumps in the sample being considered.

One can study this problem from the orthonormal basis used for the expansion of the density field. A key condition needed for the central limit theorem to hold is that the modulus of the basis be less than C/\sqrt{L} , where L is the size of the sample and C is a constant (Ivanonv & Leonenko 1989). Obviously, all Fourier-related orthonormal bases satisfy this condition because the Fourier orthonormal bases in 1-dimension are such that $(1/\sqrt{L})|\sin kx| < C/\sqrt{L}$ and $(1/\sqrt{L})|\cos kx| < C/\sqrt{L}$ and C is independent of coordinates in both physical space x and scale space k . On the

other hand, the father functions (5) have

$$|\psi_{j,l}(x)| \sim \left(\frac{2^j}{L}\right)^{1/2} \text{O}(1) \quad (7)$$

because the magnitude of the basic wavelet $\psi(x)$ is of the order 1. The condition $|\psi_{j,l}(x)| < C/\sqrt{L}$, will no longer hold for a constant C independent of scale variable j .

Aside from the Daubechies 2 wavelet (i.e.,the Haar wavelet), the father functions for the Daubechies wavelets are also localized in Fourier space. The FFC $\tilde{\delta}_{j,l}$ is only determined by the perturbations on scale j , regardless of perturbations on other scales. If the universe consists of non-Gaussian clumps on various scales j , the FFCs $\tilde{\delta}_{j,l}$ will still be effective in detecting the non-Gaussian signal. However, a measure given by a sum over a large number of scales will fail to do so.

The mother functions of the discrete wavelet transform are localized in spatial space. But the mother functions $\phi_{j,l}(x)$ are not orthogonal with respect to the scale index j , i.e. they are not localized in Fourier space (PF1, PF2). This means that the MFCs are given by a sum over perturbations on all scales larger than $L/2^j$. Thus, if the number of the independent clumps in Fourier (scale) space is large, the MFCs will also be Gaussian by the central limit theorem. The count in cell (CIC) analysis is essentially the same as the MFC. The window function of the CIC corresponds to the mother function, and the count to the amplitude of the MFCs. Like the MFCs, the CIC is scale-mixed and it may not always be sensitive to the non-Gaussian behavior on specific scales.

2.3 One-point distribution of FFCs

For the density field to be consistent with the cosmological principle, $\delta(x)$ should be described by a homogeneous random process, i.e. its probability distribution function should remain the same when x translated. On the other hand, the bases func-

tions $\psi_{j,l}(x)$ are orthogonal to translation l . Equation (6) shows that the probability distribution of $\tilde{\delta}_{j,l}$ should be l -independent.

The l -independence can also be seen from the relationship between FFC $\tilde{\delta}_{j,l}$ and Fourier coefficients δ_n (PF2) given as

$$\tilde{\delta}_{j,l} = \sum_{n=-\infty}^{\infty} \left(\frac{2^j}{L}\right)^{-1/2} \delta_n \hat{\psi}(-n/2^j) e^{i2\pi nl/2^j} \quad (8)$$

where $\hat{\psi}$ is the Fourier transform of ψ . The wavelet basis functions $\psi_{j,l}(x)$ are compactly supported in both x and Fourier space. Generally, $\hat{\psi}(n)$ will have two symmetric peaks with centers at $n = \pm n_p$, and with width Δn_p . The sum over integer n in eq.(8) need only be taken on two ranges of $(n_p - 0.5\Delta n_p)2^j \leq n \leq (n_p + 0.5\Delta n_p)2^j$ and $-(n_p + 0.5\Delta n_p)2^j \leq n \leq -(n_p - 0.5\Delta n_p)2^j$. Eq.(8) can be approximately rewritten as

$$\begin{aligned} \tilde{\delta}_{j,l} &\simeq \left(\frac{L}{2^j}\right)^{1/2} 2 \sum_{n=(n_p-0.5\Delta n_p)2^j}^{(n_p+0.5\Delta n_p)2^j} \text{Re}\{\hat{\psi}(n_p)\delta_n e^{i2\pi nl/2^j}\} \\ &\simeq \left(\frac{L}{2^j}\right)^{1/2} |\hat{\psi}(n_p)| 2 \sum_{n=(n_p-0.5\Delta n_p)2^j}^{(n_p+0.5\Delta n_p)2^j} |\delta_n| \cos(\theta_\psi + \theta_n + 2\pi nl/2^j) \end{aligned} \quad (9)$$

where we have used $\hat{\psi}(-n_p) = \hat{\psi}^*(n_p)$ and $\delta_{-n} = \delta_n^*$, because both $\psi(x)$ and $\delta(x)$ are real. θ_ψ, θ_n in eq.(9) are the phases of $\hat{\psi}(n_p)$ and δ_n , respectively. As we pointed out in last section, δ_n is Gaussian even when the clumps are non-Gaussian. The phase of δ_n, θ_n , should be uniformly randomly distributed, and therefore, from eq.(9), the probability distribution of $\tilde{\delta}_{j,l}$ is independent of l .

Moreover, if the spatial correlations of the random field $\delta(x)$ decay sufficiently rapidly with increasing separation, ranges with different l are essentially statistically independent. That is, even for one realization of $\delta(x)$, the values of FFCs $\tilde{\delta}_{j,l}$ at different l can be considered as statistically independent measurements. In other words, each FFC can be treated as independent realizations of the stochastic variable $\tilde{\delta}_{j,l}$. Thus, the FFCs, $\tilde{\delta}_{j,l}$, on scale j form an ensemble with 2^j realizations. The statistics

with respect to the one-point distribution of FFCs $\tilde{\delta}_{j,l}$ from one-realization should be equal to the results of the ensemble statistics. The goodness of this estimation is measured by the Large Number Theorem, that is, the relative error is about $1/\sqrt{2^j}$. The one-point distribution of FFCs from one-realization will be valid in detecting statistical features if density field $\delta(x)$ is ergodic: the average over an ensemble is equal to the spatial average taken over one realization.

A homogeneous Gaussian field with continuous spectrum is certainly ergodic (Adler 1981). More importantly, it has also been found that in some non-Gaussian cases, such as homogeneous and isotropic turbulence (Vanmarke, 1983), ergodicity also approximately holds. When one considers that the density field of the universe is homogeneous and isotropic, the one-point distributions of FFCs should be effective in measuring the non-Gaussianity of cosmic distributions $\delta(x)$.

2.4 Spectrum of non-Gaussianity

To take advantage of the $\tilde{\delta}_{j,l}$'s ability to detect non-Gaussian behavior at different scales, j , we define the spectrum of skewness as

$$S_j \equiv \frac{1}{N_r 2^j \sigma_j^3} \sum_{n=1}^{N_r} \sum_{l=0}^{2^j-1} [(\tilde{\delta}_{j,l} - \overline{\tilde{\delta}_{j,l}})^3]_n, \quad (10)$$

and the spectrum of kurtosis as

$$K_j \equiv \frac{1}{N_r 2^j \sigma_j^4} \sum_{n=1}^{N_r} \sum_{l=0}^{2^j-1} [(\tilde{\delta}_{j,l} - \overline{\tilde{\delta}_{j,l}})^4]_n - 3, \quad (11)$$

where the variance σ^2 is given by

$$\sigma_j^2 = \frac{1}{2^j} \sum_{l=0}^{2^j-1} (\tilde{\delta}_{j,l} - \overline{\tilde{\delta}_{j,l}})^2. \quad (12)$$

Eq.(12) is equal to $(L/2^j)P_j^{var}$ and P_j^{var} used in PF2 as the spectrum of the perturbation.

Note that eqs.(10) and (11) differ slightly from usual definition of the skewness or kurtosis by the sum over n . This is because at small j an individual sample covering

the range L will yield only a small number of $\tilde{\delta}_{j,l}$. This makes the calculation of K_j meaningless. For instance, for $j = 2$, there are only two FFCs, $\tilde{\delta}_{2,0}$ and $\tilde{\delta}_{2,1}$. In this case, $\overline{\tilde{\delta}_{j,l}} = (\tilde{\delta}_{2,0} + \tilde{\delta}_{2,1})/2$, which using the usual definition would yield $K_j = -2$ regardless of the sample or wavelet. In order to overcome this difficulty, we compile subsets consisting of N_r samples. The number of $\tilde{\delta}_{j,l}$ will then be N_r times larger than one sample making the statistics at small j viable. As with the usual definitions of skewness and kurtosis, S_j and K_j should vanish for a Gaussian distribution.

3. Demonstration of non-Gaussian detection

3.1 Normal perturbations

To ensure that eqs. (10) and (11) yielded the expected results for the Gaussian case, a 1-D density distribution $\rho(x)$ was generated from Gaussian perturbations with the following spectrum

$$P(k) = \frac{k}{1 + 10^5 k^4} \quad (13)$$

where $k = 2\pi n/L$, L being the range of the density field. The spectrum (13) has a peak at $\log k \sim -1.37$, or a typical scale at $1/k = 23.4$ (length) units.

Samples of distributions over $L = 512$ bins were produced which gave a bin size of 2π units. The reconstruction of the spectrum (13) is shown in Figure 1a. The peak and the amplitude of the power spectrum are perfectly detected by the wavelet SSD (PF2). The results of S_j and K_j are shown in Figures 1b and 1c. The error bars are given by $\sqrt{15/N}$ and $\sqrt{96/N}$, respectively, where N is the total number of wavelet coefficients, i.e., the number of realizations times 2^j . (Press et al. 1992). As expected for normal perturbations, both S_j and K_j are zero.

3.2 Distribution of clumps

Let us consider non-Gaussian density fields consisting of clumps randomly distributed in a white noise background. Clump distributions are often used to test

methods of detecting non-Gaussianity in large scale structure study (Perivolaropoulos 1994, Fan & Bardeen 1995). In fact, these kinds of studies have shown that one cannot detect the non-Gaussianity of samples by the one-point probabilities of the individual Fourier modes, even when the samples contain only a few independent clumps (Kaiser & Peacock 1991). More importantly, these distributions are necessary in studying whether random samples contain non-Gaussian signatures (see §3.3).

To begin, first note that a clump or valley with density perturbation $\Delta\rho_c$ on length scale d at position l can be described as

$$\rho^\pm(x) = \begin{cases} \pm\Delta\rho_c & \text{if } lL/2^{J_c} \leq x < (l+1)L/2^{J_c} \\ 0 & \text{otherwise} \end{cases} \quad (14)$$

where $J_c = \log_2(L/d)$, and the positive sign is for a clump, the negative sign for a valley. If a density field $\rho(x)$ consist of N randomly distributed clumps and valleys of scale d , so that the number density is $N/2^{J_c}d$ on average, the field can be realized by a random variable of density perturbation $\delta\rho$ with a probability distribution $P(\delta\rho)$ defined as

$$P[x \leq X] = \begin{cases} 0 & \text{if } X < -\Delta\rho_c \\ N/2^{J_c+1} & \text{if } -\Delta\rho_c < X < 0 \\ 1 - N/2^{J_c} & \text{if } 0 < X < \Delta\rho_c \\ 1 & \text{if } X > \Delta\rho_c \end{cases} \quad (15)$$

The distribution function $\delta\rho$ of clumps and valleys, $f_c(\delta\rho)$ can then be written approximately as

$$f_c(x) = \frac{dP}{dx} = \left(1 - \frac{N}{2^{J_c}}\right)\delta(x) + \frac{N}{2^{J_c+1}}\delta(x - \Delta\rho_c) + \frac{N}{2^{J_c+1}}\delta(x + \Delta\rho_c). \quad (16)$$

The $\delta(\cdot)$ on the right hand side of eq.(16) denote δ -functions. The characteristic function of the random variable $\delta\rho$ of clumps and valleys is

$$\phi_c(u) = \int_{-\infty}^{\infty} f(x)e^{i\delta u} dx = \frac{2^{J_c} - N}{2^{J_c}} + \frac{N}{2^{J_c}} \cos(\Delta_c u) \quad (17)$$

where $\Delta_c = \Delta\rho_c/\bar{\rho}$. It is very well known that the overall measures of skewness and kurtosis of the distribution (15) can be calculated from the characteristic function

(17). The results are

$$S = -\frac{1}{i\sigma^3} \left[\frac{d^3\phi_c(u)}{du^3} \right]_{u=0} = 0 \quad (18)$$

and

$$K = \frac{1}{\sigma^4} \left[\frac{d^4\phi_c(u)}{du^4} \right]_{u=0} - 3 = \frac{2^{J_c}}{N} - 3. \quad (19)$$

where

$$\sigma^2 = -\frac{d^2\phi_c(u)}{du^2} \Big|_{u=0} = \frac{N(\Delta_c)^2}{2^{J_c}} \quad (20)$$

is the variance of the distribution.

Consider density fields consisting of clumps or valleys randomly distributed in a background. In this case, the characteristic function is $\phi(u) = \phi_c(u)\phi_b(u)$, where $\phi_b(u)$ is the characteristic function of the background distribution. For a randomly uniform Gaussian background with variance σ_b^2 , the overall variance is

$$\sigma^2 = \frac{N(\Delta_c)^2}{2^{J_c}} + \sigma_b^2, \quad (21)$$

and the overall kurtosis is

$$K = \left(\frac{2^{J_c}}{N} - 3 \right) \left(1 + \frac{2^{J_c}}{N(s/n)^2} \right)^{-2}, \quad (22)$$

where $s/n = \Delta_c/\sigma_b$ is the signal-to-noise ratio. Eq.(22) shows that this distribution becomes Gaussian when s/n is small.

Samples of clumps and valleys randomly distributed were produced with a Gaussian noise background. Figure 2a shows a typical distribution. Here, $d = 1$ bin, there are 16 clumps and valleys on average, and the signal-to-noise ratio $s/n = 5$. The size of the distribution is $L = 512$ bins. The spectra, S_j and K_j , are shown in Figures 2b and 2c. Since the distributions are non-Gaussian, a Gaussian variance will no longer be applicable to estimate the statistical errors. Instead, the error bars in Figure 2 are calculated from the 95% confidence level from the ensemble of the samples (for each

parameter set at least 100 realizations are generated). The kurtosis calculated from the one point function of the Fourier modes has also been plotted in Figure 2. This figure clearly shows that non-Gaussian behavior can be detected by the FFCs, but not by Fourier methods.

Figure 3 shows the kurtosis spectrum for a distribution consisting of 16 randomly distributed clumps and valleys with scale $d = 4$ bins, over a length $L = 512$ bins, and $s/n = 5$. K_j is significantly different from zero on scale $j = 6$, which corresponds exactly to the scale of the clumps. i.e. $512/2^{6+1} = 4$. (The +1 in the index is due to the way scaling is counted for the FFC's. See eq. (8) and figure 1 of PF1.) This demonstrates that the scale of the clumps can be detected by the peak in the spectrum of kurtosis.

The effectiveness of detecting multiple scales of the clumps and valleys has also been tested. Figure 4 shows the results of generating samples consisting of 16, 32, and 48 clumps and valleys with a $s/n = 2.0$, and the scales of the clumps, d , are randomly distributed from 1 to 5 bins. Once again 100 realizations are generated. The kurtosis spectra are plotted in Figure 4. Also shown is the standard one value description of kurtosis, plotted for clarity of presentation at $j = 9$. This kurtosis is directly calculated from the distribution $\delta(x)$ by

$$K \equiv \frac{1}{N2^j\sigma^4} \sum_{i=1}^N [(\delta(x_i) - \overline{\delta(x_i)})^4] - 3. \quad (23)$$

Several features stand out in the Figure 4. First, the standard singled valued kurtosis is generally lower than that given by the wavelet kurtosis, especially, when the number of clumps is large. In this case the standard kurtosis totally misses the non-Gaussianity of the distribution. Second, the one value kurtosis contains a large uncertainty in detecting deviations from Gaussian behavior. This is because the distribution $\delta(x)$ is equal to about the MFCs on finest scale. As mentioned in §2.2, MFC's distributions will be Gaussian if the clumps are independent on various scales.

On the other hand, the kurtosis spectrum detected the non-Gaussian signal at $j = 6$ even when the number of clumps is as large as 48, and $s/n = 2.0$. Since the average bin width is about 3, this corresponds to about 1/3 of the 512 bins being occupied by clumps. The FFC's are extremely sensitive to deviations from Gaussian behavior.

Figure 5 directly plots the one-point distributions of the FFCs for realizations with sixteen 4d clumps and valleys over a length 512d, and with $s/n=5$. In each panel, the Gaussian distribution (dotted line) with the same variance and normalization as the FFC distribution is shown. The figure shows that the largest deviation of the distribution of FFCs from Gaussian distribution occurs on the scales of the clumps ($j = 6$).

3.3 Non-Gaussianity of random samples

In large scale structure study, the usual way of generating random distributions covering a 1-dimensional range (x_1, x_2) is

$$x_i = x_1 + (x_2 - x_1) \cdot RAN \quad (24)$$

where x_i is the position of i-th object, and RAN is random number in $(0, 1)$. Because the number of objects is an integer, the random samples given by eq.(24) easily lead to non-Gaussian distributions.

In numerical calculations, the distribution $\delta(x)$ is often binned into a histogram with a given bin size. If the bin size is less than the mean distance of neighbor objects, the value of the binned $\delta(x)$ will typically be 0 or 1. The sample is then a d=1 clump distribution with a one point distribution given by eq.(15), and *not* a Gaussian distribution. Only in the case when the mean number of objects contained in one bin is large does the one-point distribution approach the Gaussian case. To illustrate this point, Figure 6 plots the spectrum of kurtosis for a sample generated by eq.(24), in which the number of objects is 122 distributed in 64 bins. The figure

shows that the non-Gaussianity of the random sample is significant when the mean number of objects/bins is equal to 2.

Similarly, the binning of real data will lead to non-Gaussianity that is obviously not in the original distribution. Generally, in order to maximally pick up information from a real data set, the bin size is taken to be the resolution of the coordinate x , i.e. the lowest possible size of the binning. However, this data reduction will also lead to the lowest mean ratio of objects per bin and so consequently lead to the highest non-Gaussianity.

4. Non-Gaussian detection in the Ly α forests

4.1 Simulation samples of Ly α forests

The non-Gaussian behavior of samples given by simulations of the Ly α forests (Bi, Ge & Fang 1995, hereafter BGF) were examined. These samples have also been used for the demonstration of cluster identification and spectrum analysis by a wavelet SSD (PF1, PF2). The details of the simulations are given by BGF. The basic steps of the simulations are as follows: 1) generate dark matter distributions by Gaussian perturbations with a linear power spectrum of the standard cold dark matter model (SCDM), the cold plus hot dark matter model (CHDM), and the low-density flat cold dark matter model (LCDM); 2) generate the baryonic matter distribution by assuming that baryonic matter traces the dark matter distribution on scales larger than the Jeans length of the baryonic gas, but is smooth over structures on scales less than the Jeans length; 3) remove collapsed regions from the density field because Ly α clouds are probably not virialized; 4) simulate Ly α absorption spectrum as the absorption of neutral hydrogen in the baryonic gas, and include the effects of the observational instrumental point-spread-function, and along with Poisson and background noises; 5) determine the Ly α absorption line and its width from the simulated spectrum by the usual way of Ly α line identification.

Within a reasonable range of the UV background radiation at high redshift, and the threshold of the onset of gravitational collapse of the baryonic matter, the LCDM model is consistent with observational features including 1) the number density of Ly α lines and its dependencies on redshift and equivalent width; 2) the distribution of equivalent widths and its redshift dependence; 3) two-point correlation functions; and 4) the Gunn-Peterson effect. Especially important is the fact that the simulated data show no power in the two-point correlation function and that their 1-dimensional spectra is flat on scales less than $100 \text{ h}^{-1}\text{Mpc}$ (BGF, PF2).

However, no power in the two-point correlation and/or a flat spectrum does not mean that the sample is white noise. Instead, this may only indicate that the power spectrum and two-point correlation function are not suitable for describing the statistical features of the system being considered. Indeed, using a multi-resolution SSD analysis, the distributions of Ly α forest samples with no power in the two-point correlation function have been found to be significantly different from uniformly random distributions on various scales (PF1). The non-Gaussianity spectrum analysis will support this result.

As in PF1 and PF2, a one dimensional distribution $n(x)$ of the Ly α lines was formed by writing each sample into a histogram with bins on comoving scale of $2.5 \text{ h}^{-1} \text{ Mpc}$. This is about the distance at which the effect of line blending occurs. We then generated 100 uniformly random samples for each simulation sample via eq. (24). Since the lines are redshift dependent the total number of lines and the number of lines within a given red-shift interval (say, $\Delta z = 0.4$) of the random samples were chosen to match the parent distribution. We calculated the FFCs and MFCs for both the BGF sample and the random data. The original distribution $n(x)$ and its various scales of multiresolved results can perfectly be reconstructed by the MFCs (PF1).

Figure 7 gives the one-point distribution of FFCs for a SCDM sample ($W > 0.36 \text{ \AA}$). For each scale j , the corresponding Gaussian distribution is plotted such

that it has the same normalization and variance as the one-point distribution. This figure clearly shows that all the distributions on $j > 6$ (or scales less than about $40 h^{-1} \text{ Mpc}$) are significantly non-Gaussian. It is interesting to point out that the BGF simulation is based on a linear spectrum, and the perturbation field is Gaussian. The detected non-Gaussian behavior must come from the selection of high peaks in the Gaussian background fields (step 5 of the simulation procedure).

Figures 8 and 9 are the spectra of skewness and kurtosis of the SCDM samples ($W > 0.36 \text{ \AA}$). In order to test whether the detected non-Gaussianity is from the binning, Figures 8 and 9 also show the spectra of skewness and kurtosis for two random samples, I and II. Random II is produced from the Gaussian one-point distributions, which have the same normalization and variance in each j as the SCDM sample (Figure 7). As expected, the kurtosis and skewness of Random I are equal to zero. Random I is generated using eq. (24). The redshift-dependence of the number density of the Ly α lines is accounted for by generating the random data such that in each redshift range the number of lines in the random sample is the same as the SCDM sample. Hence, the spectra of the Random II samples is a measure of the possible non-Gaussianities due to the binning.

Figure 9 shows that the amplitude of the kurtosis spectrum for the SCDM sample is systematically larger than the corresponding Random I sample. Recall that the error bars in Figure 9 do not represent the 1σ Gaussian errors, but the 95% confidence level from the ensemble of the samples. The difference between the spectra of the SCDM and Random I samples is significant.

The skewness in Figure 8 is small, consistent with zero, but slightly positive. Even the Random I data has small, but positive skewness. A possible reason for the positive skewness is the redshift-dependence of number of Ly α clouds. The FFC $\tilde{\delta}_{j-1,l}$ is mainly determined by the difference of (positive) densities of $\{j, 2k\}$ and $\{j, 2k+1\}$ (PF1). Namely, for a clump in redshift space, the density change on the lower redshift

or lower k side contributes negative FFCs, while the higher redshift side give positive FFCs. If the number of Ly α clumps decreases with increasing redshift, the change in clustering amplitudes (FFCs) on the higher redshift side (positive FFCs) should be less than the lower side (negative FFCs), i.e. the number of positive FFCs will be less than negative FFCs. In Figure 7, one can see the asymmetry (non-zero skewness) in the one-point distributions.

Figure 10 and 11 give the skewness and kurtosis spectra for samples of all three models ($W > 0.16\text{\AA}$). For all models, the skewness is about the same however the kurtosis is different for different models. For the CHDM data, the K_j amplitudes are larger than that of the SCDM and LCDM data on all scales j . This is because there are far fewer high peaks in the CHDM than in SCDM and LCDM. The kurtosis is therefore a useful measure in distinguishing between the various models.

4.2 Real data

As in the first two papers (PF1 and PF2), two data sets of the Ly α forests are examined. The first was compiled by Lu, Wolfe and Turnshek (1991, hereafter LWT). It contains ~ 950 lines from the spectra of 43 QSOs that exhibit neither broad absorption line nor metal line systems. The second is from Bechtold (1994, hereafter JB), which contains a total ~ 2800 lines from 78 QSO's spectra, in which 34 high redshift QSOs were observed at moderate resolution. In our statistics, the effect of proximity to z_{em} has been considered. All lines with redshift $z_{em} \geq z \geq z_{em} - 0.15$ were deleted from our samples. We assumed $q_0 = 1/2$, so the distance of the samples range from a comoving distance from about $D_{min}=2,300 h^{-1}\text{Mpc}$ to $D_{max} = 3,300 h^{-1}\text{Mpc}$.

A problem in using real data to do statistics is the complex geometry of QSO's Ly α forest. Different forest cover different spatial ranges, and no one of the forests distributes on the entire range of (D_{min}, D_{max}) . This is a difficulty in detecting the

power spectrum by some of the usual methods. At the very least, a complicated weighting scheme is needed. However, for the wavelet SSD, this problem can easily be solved. For instance, suppose a forest sample lies in a range (D_1, D_2) . The range can be extended to (D_{min}, D_{max}) by adding zeros to the data in ranges (D_{min}, D_1) and (D_2, D_{max}) . Since the father functions are compactly supported, the FFCs in the range (D_1, D_2) will not be affected by the addition of zero in the ranges of (D_{min}, D_1) and (D_2, D_{max}) . Any statistic can then be computed by simply dropping all FFCs, $\tilde{\psi}_{j,l}$, with coordinates l in the added zero ranges. The only uncertainty due to the boundary at (D_{min}, D_{max}) are the two FFCs at boundary, $\tilde{\psi}_{j,l_1}$ and $\tilde{\psi}_{j,l_2}$, where l_1 and l_2 correspond to the positions in the regions of (D_{min}, D_1) and (D_2, D_{max}) . In PF2, we numerically demonstrated that FFCs can correctly detect the “local” spectrum, i.e. spectrum in the range (D_1, D_2) , regardless of any zero padding. In other words, the FFC spectrum reconstruction is insensitive to the selection of boundary conditions. Using this technique, all samples were extended in comoving space, to cover 1024 bins with each bin of comoving size $\sim 2.5 \text{ h}^{-1} \text{ Mpc}$. Thus, all QSO samples were treated uniformly.

Another problem in computing the spectrum of skewness and kurtosis of real data is the compilation of the subsets of the sample, needed for eqs.(10) and (11). Unlike the simulated samples, where as much data as needed can be generated, the available real data are limited. There are only $N_T = 43$ samples (forests) for LWT and 78 for JB. In order to effectively use this data, $M \leq N_T$ files from among the complete N_T samples are chosen to form a subset. Various combinations of the subsets M are then combined to form an ensemble. To investigate the effect of different combinations, the subsets M are formed by varying the total number of files chosen from the parent distribution, N_T , as well as changing the order in which the individual files are selected. It is found that the skewness and kurtosis calculated from these M -file ensembles are very stable until M contains few as 7 or 8 files, i.e. until only approximately 5% of

the total lines remain in the subset. The 95 % confidence intervals are then estimated from the ensembles.

Figure 12 gives the FFC one-point distributions for sample of $LWT > 0.36\text{\AA}$ and $JB > 0.32\text{\AA}$. As in Figure 7, these distributions show highly non-Gaussian behavior, and are also asymmetric, with fewer positive FFC's and more negative ones.

The skewness and kurtosis spectra of both the LWT and JB data are plotted in Figure 13 and 14, respectively. Even though the two data sets are independent they give the same amplitudes for the kurtosis on all scales $j > 6$ (or larger than $40 h^{-1}\text{Mpc}$). Therefore, these amplitudes are not be statistical flukes, but come from the real clustering of $\text{Ly}\alpha$ clouds. Figure 14 also show the kurtosis of samples SCDM and LCDM. In terms of second and lower order statistics, such as number density and two-point correlation functions, LCDM gives best fitting of observed data. However, LCDM's kurtosis are found to be systematically less than real data.

To check for non-Gaussianity due to binning, Figures 15 and 16 give the skewness and kurtosis spectra of the JB ($W > 0.16\text{\AA}$) sample and its Random I data. The Random I samples have the same number density as the $\text{Ly}\alpha$ lines in each redshift ranges $\Delta z = 0.4$ as the real data. The difference of kurtosis between the JB and its Random I sample (Figure 16) is more significant than the difference between SCDM and its Random I data (Figure 9). This indicates that real data is more non-Gaussian than the linear simulation sample.

As in Figure 8, all the skewness of LWT, JB and JB's Random I are consistent with zero, but slightly positive. This is probably because the positive evolution of the number of $\text{Ly}\alpha$ clusters with redshift.

5 Discussion and conclusions

We have demonstrated that the one-point distribution of FFCs of the discrete wavelet is a good tool for detecting non-Gaussian behavior in cosmic density fields.

The locality of the wavelet farther functions in both configuration and Fourier spaces allows for a way around the central limit theorem: a superposition of randomly distributed non-Gaussian clumps will be Gaussian.

It is generally believed that the ergodic hypothesis is reasonable if spatial correlations are decreasing sufficiently rapidly with increasing separation. In this case, volumes separated with distances larger than the correlation length can be considered as statistically independent regions. Therefore, in terms of short-range correlated components, such volumes can be treated as independent realizations. Many theoretical models indeed predict that the perturbations in the universe are short-range correlated, or, at least, that the universe contains short-range correlated components. The wavelet FFCs effectively measure these statistically independent regions. Thus, in the case where the “fair sample hypothesis” (Peebles 1980) holds, the FFC one-point distribution taken from one-realization is a fair estimate of the PDF of density fields.

The spectra of skewness and kurtosis provide a systematic and uniform measure of the non-Gaussianity of various samples. This method is sensitive to samples containing many clumps embedded in a Gaussian background, while Fourier methods fail to do so (Perivolaropoulos 1994). As opposed to the PDF given by CIC, which is statistically incomplete, the FFCs give a complete description of the scale-dependence of the skewness and kurtosis.

The spectra of skewness and kurtosis have been detected for QSO’s Ly α forests in both observational and linearly simulated samples. In previous studies these samples have shown no power in the two-point correlation function and a flat power spectrum. The results of the non-Gaussian detection are non-trivial: all distributions are found to be non-Gaussian on at least scales of less than 40 h $^{-1}$ Mpc, and the non-Gaussianities are not completely due to the effects of binning. It is clear that high order statistics, such as the spectrum of the kurtosis, can indeed provide information which is missed

by the 2nd order statistics. The amplitude and shape of the kurtosis spectrum are found to be the same for the two independent data sets. Thus, the features shown in the kurtosis spectrum should come from the formation and evolution of Ly α clouds. We will study the dynamical implication of these features in future work.

The kurtosis spectrum for the BGF simulation samples of Ly α forests was also calculated. The kurtosis spectra are different for different dark matter models describing the formation of Ly α clouds. Among the BGF samples, the best fitting to the observed number density and its evolution of Ly α clouds is given by the LCDM data. However, the kurtosis spectrum of the LCDM sample is significantly lower than real data. This result is consistent with that given by cluster identification. In PF1, it was found that the ratio between the numbers of larger and lower scale clusters for the real data is greater than that of the LCDM data. Obviously, the larger the cluster number ratio, the larger the deviation from a Gaussian distribution. Hence, the kurtosis and skewness spectrum opens a new window for looking at the statistical features of large scale structures. It is an important addition to the existing methods of describing the clustering and correlation of the cosmic density field, and for discriminating among models of structure formation.

Both authors wish to thank Professor P. Carruthers, and Drs.H.G. Bi and P. Lipa for insightful conversations.

References

- Adler, R.J. 1981, *The Geometry of Random Field*, (New York, Wiley)
- Alimi, J.M., Blanchard, A. & Schaeffer, R. 1990, ApJ, 402, 38
- Bouchet, F., Strauss, M.A., Davis, M., Fisher, K.B., Yahil, A. & Huchra, J.P. 1993, ApJ, 417, 36
- Bechtold, J. 1994, ApJS, 91, 1.
- Bi, H.G., Ge, J. & Fang, L.Z. 1995, ApJ, 452, 90, (BGF)
- Daubechies, I., 1992, *Ten Lectures on Wavelets*, SIAM
- Duncan, R.C., Ostriker, J.P. & Bajtlik, S. 1989, ApJ, 345, 39
- Fan Z.H. & Bardeen, J.M. 1995, astro-ph/9505017
- Fang, L.Z. 1991, A&A, 244, 1
- Farge, M., 1992, Ann. Rev. Fluid Mech., 24, 395
- Feldman, H.A., Kaiser N. & Peacock, J.A. 1994, ApJ 426, 23.
- Gaztañaga, E. & Frieman, J. 1994, Astrophys. J. Lett. 437, L13
- Gaztañaga, E. & Yokoyama, J. 1993, ApJ, 403, 4
- Hamilton, A.J.S. 1985, ApJ, 292. L35
- Ivanov, A.V. & Leonenko, N.N. 1989, *Statistical Analysis of Random Field*, Klumer Academic Pub.
- Juszkiewicz, R., Bouchet, F.R. & Colombi, S. 1993, ApJ, Lett, 412, L9
- Kaiser, N. & Peacock, J.A. 1991, ApJ, 379, 482
- Kofman, L., Bertschinger, E., Gelb, M.J., Nusser, A. & Dekel, A. 1994, ApJ, 420, 44
- Liu X.D., Jones B.J.T. 1990, MNRAS, 242, 678
- Lu, L., Wolfe, A.M., & Turnshek, D.A. 1991, ApJ, 367, 19 (LWT)
- Meyer, Y. 1993, *Wavelets: Algorithms and Applications*, SIAM
- Pando, J. & Fang, L.Z. 1996, ApJ, 459, 1 (PF1)
- Pando, J. & Fang, L.Z. 1995, astro-ph/9509032 (PF2)

- Peebles, P.J.E. 1980, *The Large Scale Structure of the Universe*, Princeton Univ. Press
- Perivolaropoulos, L. 1994, MNRAS, 267, 529
- Press, W.H., Flannery, B.P., Teukolsky, S.A. & Vetterling, W.T., 1992, *Numerical Recipes*, Cambridge
- Suginohara, T. & Suto, Y. 1991, ApJ, 371, 470
- Vanmarke, E.H. 1983, *Random Field*, MIT
- Yamada, M. & Ohkitani, K. 1991, Prog. Theor. Phys., 86, 799

Figure captions

Figure 1 Spectra of skewness and kurtosis for Gaussian perturbations with perturbation spectrum $P(k) = k/(1 + 10^5 k^4)$, which has a peak at $\log k \sim -1.37$, where $k = 2\pi n/L$, L being the range of the sample. The samples are produced over $L = 1024$ bins, and the bin size is 2π units. a.) the reconstructed spectrum $P(k)$, b.) S_j and c.) K_j . The error bars are given by $\sqrt{15/N}$ for the skewness, and $\sqrt{96/N}$ for the kurtosis, where N is the number of wavelet coefficients.

Figure 2 Spectra of skewness and kurtosis for clump distribution, which consist of sixteen d clumps and valleys randomly distributed in a Gaussian noise background. The length of the distribution is $L = 512d$, and signal-to-noise ratio s/n is 5. a) A typical realization of the distribution; b) S_j ; c) K_j ; and d) the kurtosis calculated from one point function of FFT.

Figure 3 Spectra of skewness and kurtosis for clump distribution, consisting of 16 randomly distributed clumps and valleys with scale $d = 4$ bins, and over a length $L = 512$ bins. s/n is 5.

Figure 4 Kurtosis spectra for samples consisting of 16, 32, and 48 clumps. The sizes of the clumps, d , are randomly distributed in range of 1 to 5 bins. s/n is 2, and the length of the sample is $L = 512$ bins.

Figure 5 Histogram of the one-point distribution of FFCs for a clump distribution consisting of 16 clumps and valleys with $d = 4$ bins in range $L = 512$ bins, and $s/n = 5$. The vertical coordinate is relative. At each scale j , the Gauss distribution (dashed line) has the same variance and normalization as the FFC distribution.

Figure 6 Spectrum of kurtosis of 120 objects randomly distributed in 64 bins.

Figure 7 Histogram of the one-point distribution of FFCs for a BGF sample in SCDM model. The width of the Ly α lines is $\geq 0.36\text{\AA}$. The vertical coordinate is the number of FFCs. At each scale j , the Gaussian distribution (dashed line) has the same variance and normalization as the FFC distribution.

Figure 8 Skewness spectrum of BGF sample of SCDM model. The solid and dashed lines are the spectra of Random I and Random II samples, respectively.

Figure 9 Kurtosis spectrum of BGF sample of SCDM model. The solid and dashed lines are the spectra of Random I and Random II samples, respectively.

Figure 10 Skewness spectrum of BGF samples in the SCDM, LCDM and CHDM with $W \geq 0.16\text{\AA}$.

Figure 11 Kurtosis spectrum of BGF samples in the SCDM, LCDM, and CHDM with $W \geq 0.16\text{\AA}$.

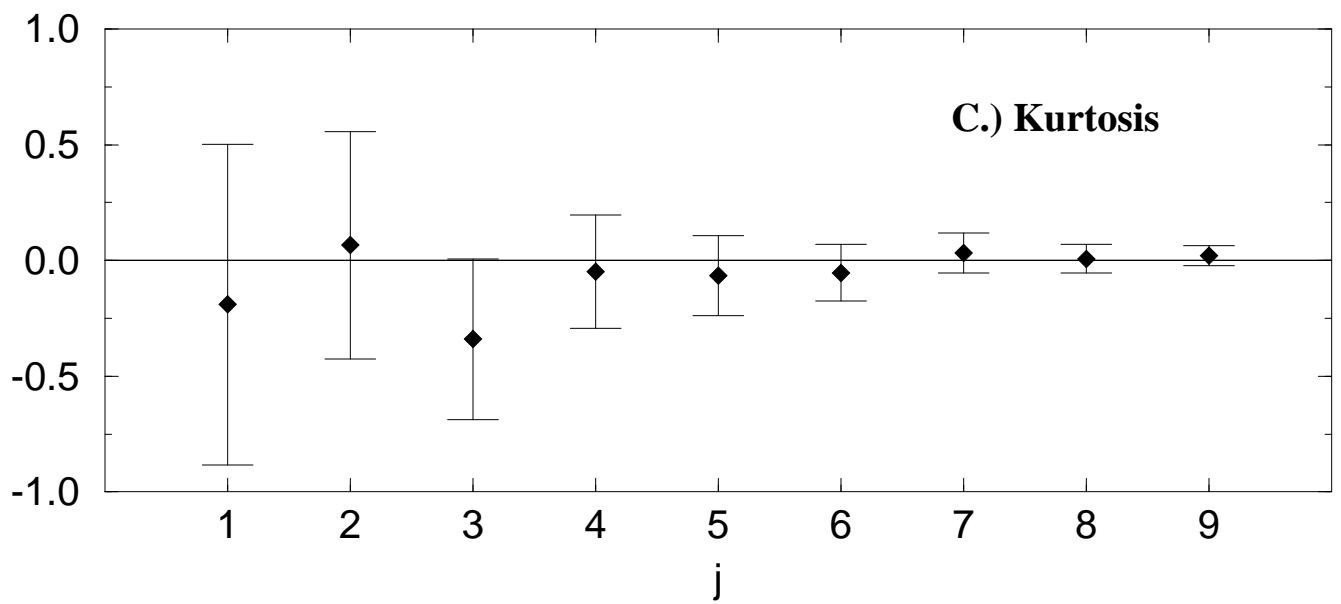
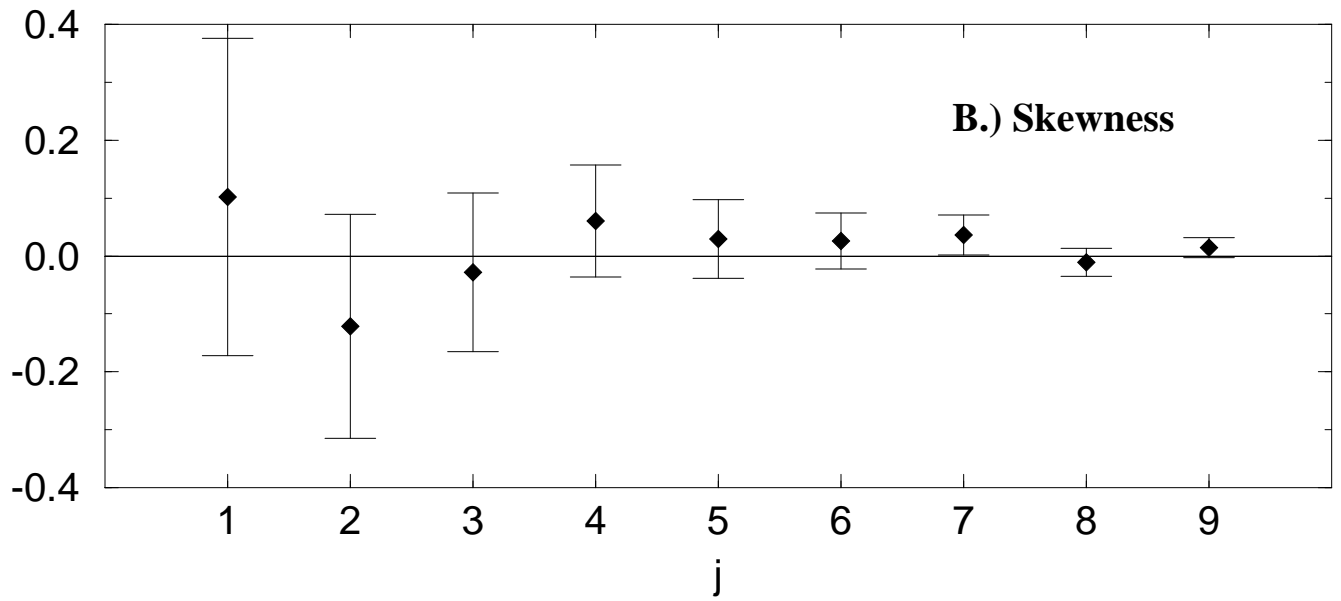
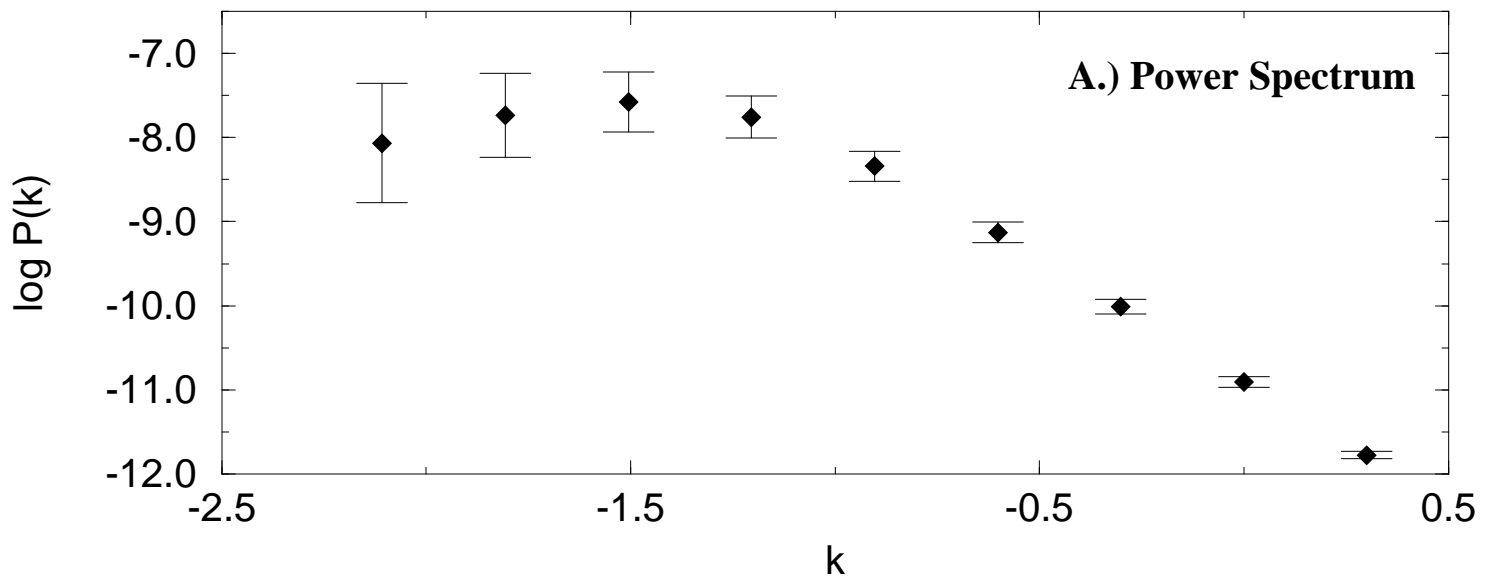
Figure 12 Histogram of one-point distribution of FFCs for samples of LWT ($W > 0.36\text{\AA}$) and JB ($W > 0.32\text{\AA}$). The vertical coordinate is relative. At each scale j , the Gauss distribution (dashed line) has the same variance and normalization as the FFC distribution.

Figure 13 Skewness spectrum for LWT and JB data.

Figure 14 Kurtosis spectrum for LWT and JB data. For comparison, the corresponded K_j of the SCDM and LCDM are also plotted. The width of lines is $> 0.16\text{\AA}$.

Figure 15 Skewness spectra for JB data ($W > 0.16\text{\AA}$), and its Random II sample.

Figure 16 Kurtosis spectra for JB data ($W > 0.16\text{\AA}$), and its Random II sample.



A.)

